Research on Chemical Intermediates
https://doi.org/10.1007/s11164-018-3611-x

Synthesis, structure, computational modeling, and biological activity of two novel bimesitylene derivatives

Lucian G. Bahrin[1] · Lilia Clima[1] · Sergiu Shova[1] · Irina Rosca[1] · Corneliu Cojocaru[1] · Dana Bejan[1] · Monica C. Sardaru[1] · Narcisa Marangoci[1] · Vasile Lozan[1,2] · Alexandru Rotaru[1]

Received: 10 July 2018 / Accepted: 24 September 2018

Abstract
Tetrazole- and nitrile-containing bimesitylene derivatives with potential use in coordination chemistry were synthesized and characterized, and their structural particularities are discussed. For the bimesitylene bistetrazole derivative, geometry optimization was carried out by quantum-chemical calculations using density functional theory together with vibrational frequencies, natural bond orbitals, and highest occupied molecular orbital (HOMO)–lowest unoccupied molecular orbital (LUMO) calculations. The newly synthesized bimesitylene derivatives were also evaluated for their antimicrobial activity against three different reference strains, namely *Escherichia coli*, *Staphylococcus aureus*, and *Candida albicans*.

Keywords Bimesitylene derivatives · Tetrazole · DFT · HOMO–LUMO · Antimicrobial activity

Introduction

Biaryls are an important class of derivatives and intermediates, found in many natural products, such as alkaloids, biologically active compounds (drugs, pesticides, etc.), and dyes [1]. Moreover, the emergence of metal–organic frameworks as promising materials with a host of remarkable properties [2] has led to an increase in the synthesis of functionalized biaryls capable of coordinating metal centers. Bimesitylene, in particular, is an interesting molecule due to the two aromatic rings being

✉ Alexandru Rotaru
rotaru.alexandru@icmpp.ro

[1] "Petru Poni" Institute of Macromolecular Chemistry, Romanian Academy, 700487 Iasi, Romania

[2] Institute of Chemistry of Moldova Academy of Sciences, 2028 Chişinău, Republic of Moldova

Published online: 01 October 2018

perpendicular to each other for steric reasons. This means that the four aromatic hydrogen atoms are arranged at the corners of a tetrahedron, and substituting them could potentially lead to derivatives capable of forming three-dimensional (3D) networks [3]. Currently, only a few functionalized bimesitylene derivatives are known, including carboxyl-, formyl-, nitrile-, or ethynyl-bearing derivatives [4, 5]. Increasing the number of readily coordinating functionalities grafted onto the bimesitylene core may prove beneficial not only in the field of metal–organic frameworks, but also for development of new compounds with interesting biological properties. An increasingly popular functionality, the tetrazole moiety with its electron-rich planar structural features, has found many uses in pharmaceutical drugs (antibacterial, antiallergic, antiinflammatory, and antifungal) [6], not to mention the recent increase in use of tetrazole rings as building blocks for design and preparation of functional metal–organic frameworks [7–9] and metal–organic zeolites [10, 11].

We present herein the synthesis, spectral data, as well as X-ray structure of two new bimesitylene derivatives, including one structure bearing two tetrazole moieties, with potential uses in coordination chemistry. To better understand the structure–activity relationship of the new bimesitylene bistetrazole molecule, geometry optimization was carried out using quantum-chemical calculations with density functional theory (DFT), together with vibrational frequencies, natural bond orbitals, and HOMO–LUMO calculations. The DFT method was chosen due to its great accuracy and efficiency [12–14]. Moreover, it is known that the DFT method adequately takes into consideration electron correlation contributions, which are especially important in systems containing extensive electron conjugation [15]. Besides these theoretical investigations, the newly synthesized bimesitylene derivatives were also tested, and their antimicrobial activity evaluated against three different reference strains, namely *Escherichia coli*, *Staphylococcus aureus*, and *Candida albicans*, revealing that the tetrazole-containing derivative selectively inhibited yeast growth.

Results and discussion

Synthesis

Synthesis of the target compounds was performed according to Scheme 1.

The first step involved homocoupling of mesitylenemagnesium bromide in presence of iron(III), as previously described [16]. In our case, however, Grignard reagent was generated using magnesium turnings and bromomesitylene **1** in refluxing tetrahydrofuran (THF), over a period of 2 h. Upon workup, bimesitylene **2** was obtained as colorless crystals in 60% yield. The next step involved iodination of **2** using molecular iodine in nitric acid/sulfuric acid mixture [3]. This afforded 3,3′,5,5′-tetraiodobimesitylene **3** in 85% yield, upon recrystallization of the raw reaction product from chloroform.

Treatment of iodinated product **3** with copper(I) cyanide afforded the desired 3,3′,5,5′-tetracyanobimesitylene **4**. The reaction was performed in dimethylformamide (DMF) over 24 h at 140 °C, and the desired product was obtained in 70% yield.

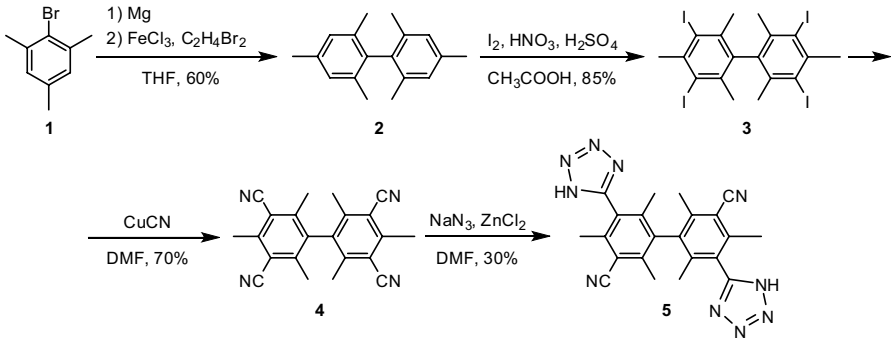

Scheme 1 Synthetic pathways for preparation of bimesitylene bistetrazole **5**

Formation of **4** was supported by spectral data. Thus, the ^{13}C nuclear magnetic resonance (NMR) spectrum of **4** indicated disappearance of the signal at 105.3 ppm, corresponding to the four carbon atoms involved in the C–I bonds. Instead, two new signals were found at 114.5 and 115.4 ppm, corresponding to the aromatic carbon atoms bound to the CN groups and the carbon atoms of the CN groups, respectively. The IR spectrum of **4** revealed the presence of a strong signal at 2224 cm^{-1}, attributed to CN groups. Single crystals suitable for X-ray diffraction were obtained by layering pentane over a solution of **4** in dichloromethane.

Cyclization of **4** to bistetrazolyl derivative **5** was performed with sodium azide and zinc chloride in DMF at 150 °C over 72 h. The relatively low yield of 30% and the formation of only bistetrazolyl derivative are probably due to a number of factors, including the steric hindrance of the nitrile groups and the relatively elevated temperature over a long period of time, which probably caused some decomposition of the reaction product. In a separate attempt, we increased the reaction time to 7 days, however, after workup, we were left with a brown residue from which no single product could be isolated, suggesting that prolonged heating of the tetrazolyl derivatives led to their decomposition. The ^{1}H NMR spectrum of **5** displayed the presence of the tetrazole proton as a broad singlet at 16.85 ppm, while the ^{13}C NMR spectrum revealed the presence of a new signal at 153.3 ppm, attributed to the tetrazole carbon atom. In the IR spectrum of **5**, a new broad signal appeared at 3497 cm^{-1}, corresponding to the N–H groups, as well as the crystallization water molecules. Single crystals suitable for X-ray diffraction were obtained through recrystallization from ethanol.

X-ray analysis

The structure of compounds **4** and **5** in solid state was studied by single-crystal X-ray diffraction analysis. Accordingly, compound **4** crystallizes in space group $P2_1/n$ of monoclinic system with one molecular unit of 3,3′,5,5′-tetracyanobimesitylene in the asymmetric part, as shown in Fig. 1. As expected, the steric effect caused by the positions of the methyl groups determines a nonplanar conformation of the molecule, with dihedral angle between two aromatic rings of 91.74(8)°.

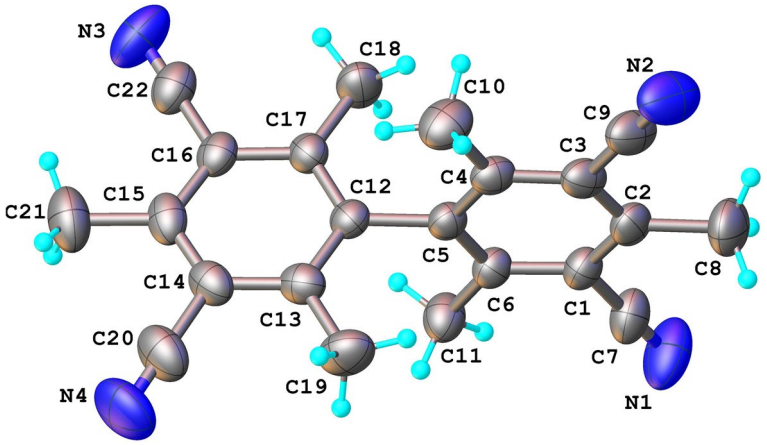

Fig. 1 X-ray molecular structure of **4** with atom labeling and thermal ellipsoids at 50% probability level

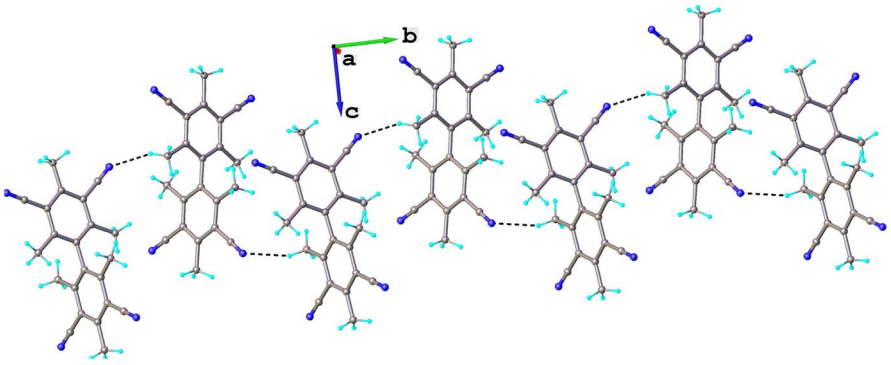

Fig. 2 One-dimensional supramolecular chain in crystal structure of **4**. H-bond parameters: C19–H···N2 [C19–H, 0.96 Å; H···N2, 2.60 Å; C19···N2 (1.5 – *x*, *y* – 0.5, 0.5 – *z*); ∠C19HN2 155.2°

The crystal packing shows the presence of one-dimensional (1D) supramolecular chains running along the *b* axis, sustained by weak H-bonding between CH_3 as donors and nitrile groups as acceptors of protons. The formation of a one-dimensional chain is shown in Fig. 2.

On the other hand, compound **5** crystallizes in *C2/c* space group of monoclinic system. It exhibits a molecular crystal structure comprising bistetrazolybimesitylene and water molecules in 1:2.5 ratio. X-ray analysis of compound **5** showed that the molecule exhibits proper symmetry with twofold axis crosses through the center of C4–C4′ bond (Fig. 3). Two symmetrically related aromatic rings are almost perpendicular, being rotated around the common bond at 88.7°, which is close to that observed for compound **4**. The dihedral angle of the planes described by the phenyl and tetrazole rings is 113.2°.

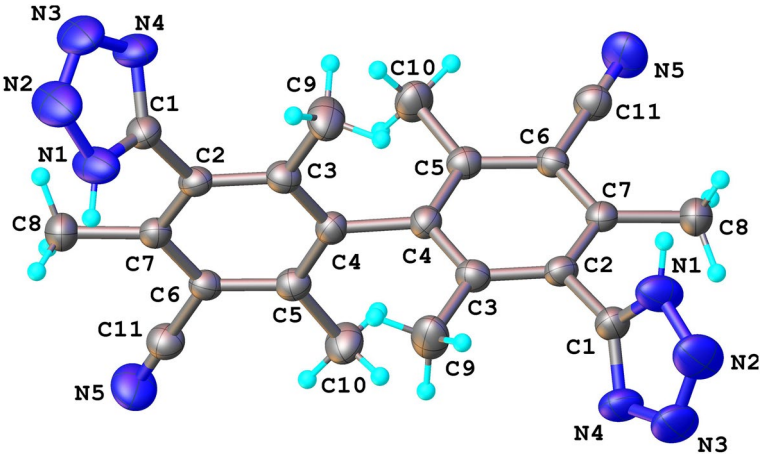

Fig. 3 X-ray molecular structure of compound **5** with atom labeling and thermal ellipsoids at 50% level

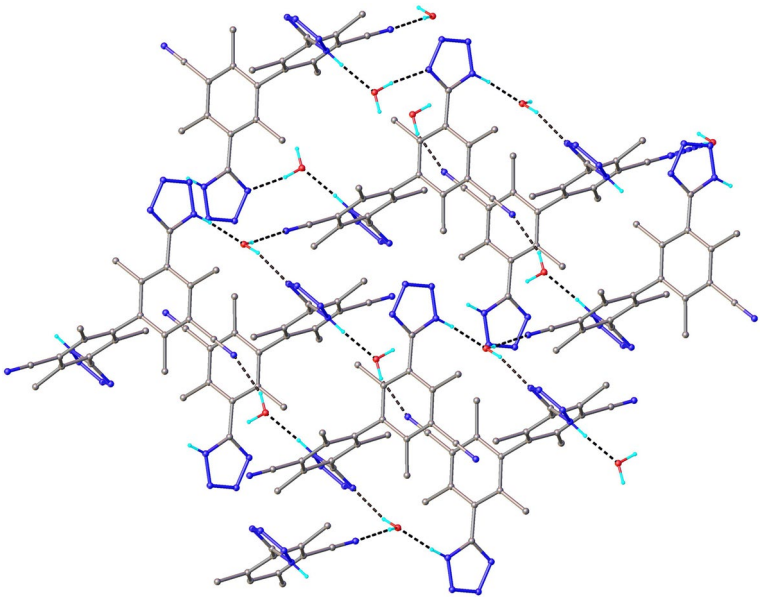

Fig. 4 Partial view of three-dimensional supramolecular network in the crystal structure of **5**. H-bond parameters: N1–H···O1*w* [N1–H, 0.86 Å; H···O1*w*, 1.85 Å; N1···O1*w* (*x*, –*y*, 0.5 + *z*) 2.702(3) Å; ∠N1HO1*w*, 173.4°]; O1*w*–H···N4 [O1*w*–H, 0.85 Å; H···N4, 2.04 Å; O1*w*···N4 (0.5 – *x*, 0.5 – *y*, –*z*), 2.874(3) Å; ∠O1*w*HN4, 164.9°]; O1*w*–H···N5 [O1*w*–H, 0.85 Å; H···N5, 2.12 Å; O1*w*···N5 (0.5 – *x*, 0.5 – *y*, –*z*), 2.930(3) Å; ∠O1*w*HN5, 158.8°]

In the crystal, the components of the structure interact via a O–H···N and N–H···O hydrogen-bonding system to form a three-dimensional supramolecular network, as shown in Fig. 4.

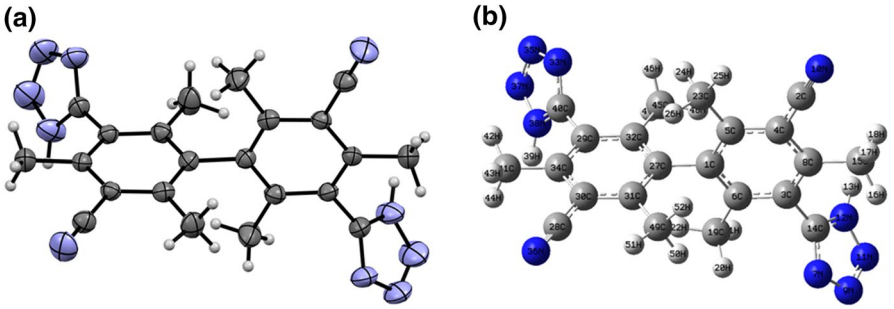

Fig. 5 Illustration of observed and theoretical molecular structure of compound **5**: **a** single-crystal X-ray structure (ORTEP view), thermal ellipsoids drawn at 50% probability level; **b** optimal geometry computed by DFT/B3LYP/6-31+G** method in ground state (all atoms numbering)

A perspective view of molecule **5**, together with the data on geometry optimization and structural aspects, are presented and discussed below.

Geometry optimization and structural aspects of compound 5

Generally, the first point of quantum-chemical calculations requires optimization of the molecular geometry by energy minimization. In this study, we applied B3LYP/6-31+G** and LSDA/6-31+G** methods for geometry optimization of compound **5**. The DFT-optimized structures were compared with the observed one (X-ray crystal) in terms of root-mean-square deviation (RMSD), a measure of the similitude between the observed crystal structure and the predicted geometry of a molecule in terms of atomic positions. The smaller the RMSD, the better the goodness of fit between the experimental (X-ray) and predicted (DFT) molecular structure. The explicit mathematical expression for the RMSD estimator is given elsewhere [17, 18].

The single-crystal structure determined by X-ray analysis is shown in Fig. 5a, along with the molecular geometry optimized at B3LYP/6-31+G** level (Fig. 5b). Full atomic numbering is given for the DFT-optimized geometry (Fig. 5b), as reference labels for comparison of both structures.

Table 1 presents selected structural parameters (bond lengths, valence, and torsion angles) for comparison between the crystal structure and the predicted molecular geometry of compound **5**. The data in Table 1 reveal reasonable agreement between the crystal structure and predicted geometries (B3LYP/6-31+G** and LSDA/6-31+G**) in terms of structural parameters.

An explicit comparison between the single-crystal structure and DFT-predicted geometry is highlighted in Fig. 5, detailing the overlapping plots and corresponding RMSD values.

As shown in Fig. 6a, the optimized conformation (B3LYP/6-31+G**) fitted well with the crystal structure. Likewise, Fig. 6b exhibits the computed geometry (LSDA/6-31+G**) and the match with the observed structure (X-ray). The overlap between the experimental and predicted structure reveals an enhanced RMSD

Table 1 Summary of selected structural parameters: bond lengths (Å), valence angles (°), and torsion angles (°), for the investigated compound **5**

Geometry/structural parameter[a]	Exp. (X-ray)	B3LYP/6-31+G**	LSDA/6-31+G**
b(1C–27C)	1.504(3) Å	1.505 Å	1.481 Å
b(2C–4C)	1.445(3) Å	1.436 Å	1.418 Å
b(2C≡10N)	1.143(4) Å	1.164 Å	1.171 Å
b(3C–14C)	1.479(3) Å	1.480 Å	1.454 Å
b(14C–12N)	1.330(4) Å	1.354 Å	1.351 Å
b(12N–13H)	0.860(0) Å	1.011 Å	1.021 Å
b(12N–11N)	1.336(3) Å	1.351 Å	1.337 Å
b(11N–9N)	1.285(4) Å	1.292 Å	1.294 Å
b(9N–7N)	1.356(3) Å	1.361 Å	1.341 Å
b(7N–14C)	1.308(3) Å	1.324 Å	1.329 Å
b(6C–19C)	1.517(4) Å	1.513 Å	1.486 Å
b(8C–15C)	1.499(3) Å	1.511 Å	1.489 Å
∠(4C–2C–10N)	179.5(3)°	179.04°	179.60°
∠(3C–14C–12N)	124.0(2)°	125.41°	126.41°
∠(3C–14C–7N)	128.1(2)°	127.39°	127.27°
∠(7N–14C–12N)	107.8(2)°	107.19°	106.32°
τ(31C–27C–1C–5C)	−91.7(3)°	−92.41°	−97.15°
τ(32C–27C–1C–6C)	−91.4(3)°	−93.97°	−100.33°
τ(8C–3C–14C–7N)	113.1(3)°	110.80°	142.25°
τ(6C–3C–14C–7N)	−68.1(3)°	−68.20°	−37.14°

[a]*b*, bond; ∠, valence angle; *τ*, torsion angle

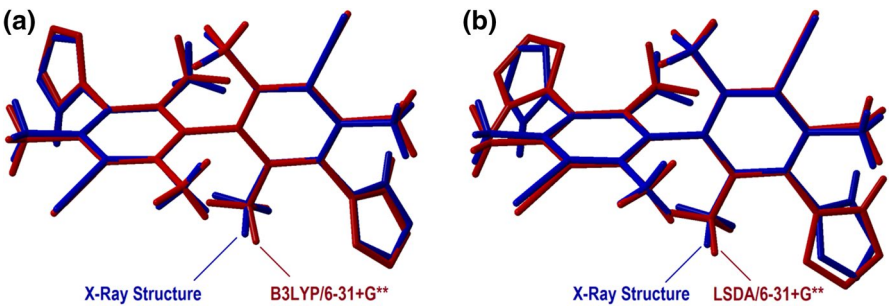

Fig. 6 Comparison between observed and theoretical structure of **5** by overlapping; X-ray structure (blue), and theoretical structures (red) computed by different methods: **a** B3LYP/6-31+G** (RMSD = 0.211 Å) and **b** LSDA/6-31+G** (RMSD = 0.354 Å). (Color figure online)

value (0.211 Å) for the B3LYP/6-31+G** model, compared with the LSDA/6-31+G** one (RMSD = 0.354 Å). Hence, the hybrid functional B3LYP was better at predicting the structural parameters of compound **5** in comparison with the local spin-density approximation (LSDA); For example, according to X-ray structure

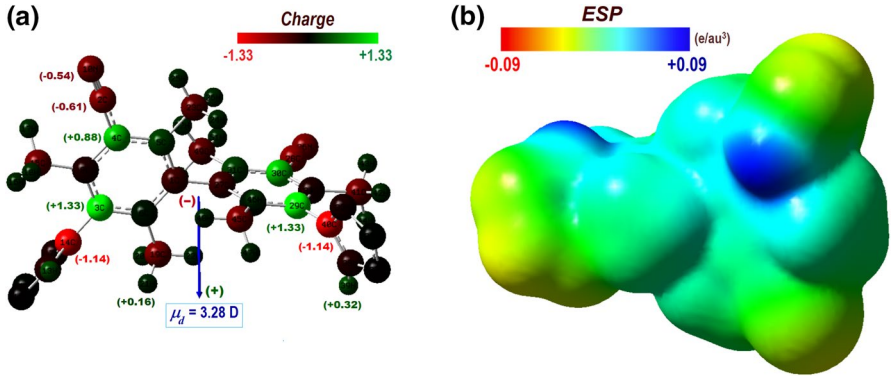

Fig. 7 Electrostatic properties of molecule **5**: **a** partial atomic charge distribution along with the dipole moment orientation and **b** electrostatic potential surface map; computation performed at B3LYP/6-31+G** level

analysis, the torsion angle (6C–3C–14C–7N) was −68.1°, while the prediction given by B3LYP/6-31+G** was very close, i.e., −68.20° (Table 1). In turn, for the same dihedral (6C–3C–14C–7N), the LSDA/6-31+G** method suggested a value of −37.14° (Table 1), thereby revealing a greater deviation from the observed value. Consequently, we adopted the B3LYP/6-31G** level of theory as the principal method to perform additional analysis of molecule **5**.

Population analysis, HOMO–LUMO calculation, and reactivity descriptors

In computational chemistry, population analysis provides the distribution of the partial atomic charges that influence molecular properties such as the electrostatic potential, dipole moment, polarizability, vibration modes, and donor–acceptor behavior [15].

For compound **5**, the distribution of partial atomic charges (Mulliken) was calculated at B3LYP/6-31+G** level and is shown in Fig. 7a. In this diagram, the partial atomic charge values are highlighted using a color map. The dipole moment orientation (3.28 D) is rendered as a vector with origin at the biphenyl core (Fig. 7a).

As detailed in Fig. 7a, two carbon atoms (from the tetrazole moieties) have the most intense negative charge ($\delta_{14C} = -1.14$, $\delta_{40C} = -1.14$). In turn, the highest positive charges are attributed to carbons from phenyl groups that are directly connected to tetrazole moieties ($\delta_{3C} = +1.33$, $\delta_{29C} = +1.33$).

On the basis of the atomic charge distribution, the electrostatic potential surface (ESP) surrounding molecule **5** was calculated by integration techniques. Figure 7b illustrates the mapped isosurface of ESP computed at B3LYP/6-31+G** level. In this graph, the highest positive ESP regions (blue spots) can be distinguished near the hydrogen atoms (>N–**H**) from tetrazole moieties, suggesting sites for nucleophilic attack. The moderately negative ESP areas are depicted in Fig. 7b as yellow-spotted regions that may be discerned near –N=N– bond (in tetrazole) and around nitrile groups (–C≡N).

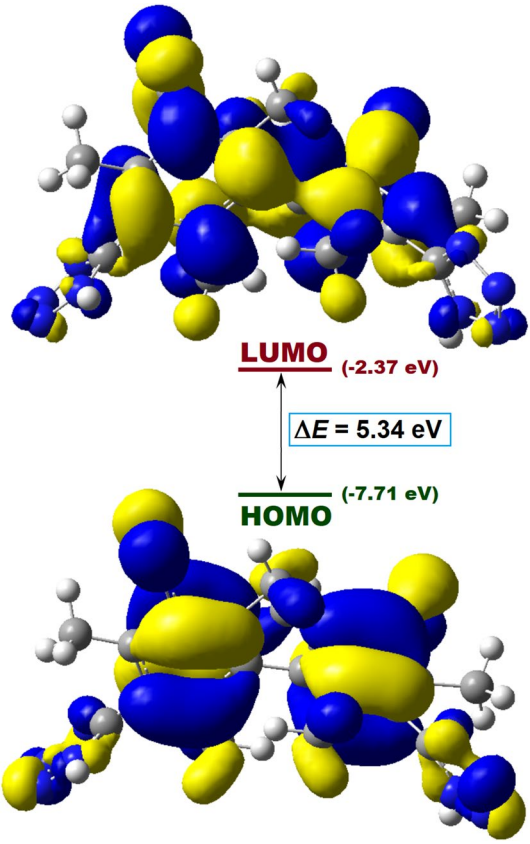

Fig. 8 Rendering of frontier molecular orbitals (HOMO–LUMO) patterns and associated bandgap energy value for molecule **5** (in gas phase); computations performed at B3LYP/6-31+G** level

The patterns of the frontier molecular orbitals (HOMO, LUMO) are depicted in Fig. 8. According to the B3LYP/6-31+G** method, the bandgap energy (HOMO–LUMO) was equal to 5.34 eV.

As shown in Fig. 8, the orbital lobes of both the HOMO and LUMO are delocalized over the entire molecule, i.e., on the diphenyl core, tetrazole moieties, and nitrile groups. Such a pattern of molecular orbitals suggests strong intramolecular electronic conjugation (i.e., a π–π conjugated system).

In addition, we calculated the molecular and reactivity descriptors for molecule **5** according to the methodology presented elsewhere [19–21]. These results related to molecular properties and global reactivity descriptors are summarized in Table 2.

Thus, the computational results reveal that molecule **5** belongs to point group (symmetry) *C1*, bestowing a molecular surface of 422 $Å^2$ with heat of formation and polarizability volume equal to 200.73 (kcal/mol) and 48.15 $Å^3$, respectively. Regarding the global chemical reactivity of molecule **5**, the following descriptors were calculated: electronegativity of 5.041 eV, chemical hardness of 2.67 eV, electrophilicity of 4.76 eV, and chemical softness of 0.187 eV^{-1}. Note that the

Table 2 Summary of molecular and global reactivity descriptors for compound **5**; descriptors computed mainly at B3LYP/6-31+G** level of theory

Molecular/reactivity descriptor	Computed value
Empirical formula	$C_{22}H_{20}N_{10}$ (52 atoms, 222 electrons)
Molecular point group (symmetry)	*C1*
Dipole moment (Debye)	3.2845
Max. molecular dimension (Å)	11.525
Molecular surface area (vdW) (Å^2)	421.98
Solvent-accessible surface area (SAS) (Å^2)	592.64
Molecular volume (from SAS) (Å^3)	1028.59
Heat of formation (kcal/mol)[a]	200.73
Polarizability volume (Å^3)[a]	48.15
LUMO eigenvalue, ε_{LUMO} (eV)	−2.372
HOMO eigenvalue, ε_{HOMO} (eV)	−7.711
Energy gap, $\Delta E = \varepsilon_{LUMO} - \varepsilon_{HOMO}$ (eV)	5.339
Ionization potential, $I \approx -\varepsilon_{HOMO}$ (eV)	7.711
Electron affinity, $A \approx -\varepsilon_{LUMO}$, (eV)	2.372
Electronegativity, $\chi = ½(I + A)$ (eV)	5.041
Chemical potential, $\mu = -\chi$ (eV)	−5.041
Chemical hardness, $\eta = ½(I - A)$ (eV)	2.670
Chemical softness, $S = ½\eta$ (eV^{-1})	0.187
Electrophilicity index, $\omega = \mu^2/2\eta$ (eV)	4.76
Electron-donating power, $\omega^- = (3I + A)^2/16(I - A)$ (eV)	7.614
Electron-accepting power, $\omega^+ = (I + 3A)^2/16(I - A)$ (eV)	2.573

[a]Computed by PM7 semiempirical method (MOPAC)

electron-accepting power of **5** was equal to 2.573 eV, which might be correlated with the sites for nucleophilic attack identified on the ESP (Fig. 3b). In contrast, the electron-accepting power of molecule **5** was equal to 7.614 eV, which might be associated with the presence of lone-pair electrons from nitrogen atoms.

Antimicrobial activity

The antimicrobial activity was measured by agar disk diffusion method, which consists in adding each tested compound to culture medium, preinoculated with microbial suspension, and measuring the inhibition zone after 24 h of incubation. The tested compounds **4** and **5** showed no antibacterial activity against the reference strains *S. aureus* and *E. coli*, but compound **5** proved to show selective antifungal activity against *C. albicans*, especially at concentration of 20 mg/mL. Data on the average diameters of the inhibition zones are presented in Table 3.

Analyzing the obtained results reveals that intermediate **4** did not show any antimicrobial activity against *C. albicans* in comparison with compound **5**. This can

Table 3 Antimicrobial activity of compounds against reference strains (mm)

Compound concentration (mg/mL)	Strain													
	Inhibition zone of **4** (mm)							Inhibition zone of **5** (mm)						
	20	10	5	2.5	1.25	0.63	0.31	20	10	5	2.5	1.25	0.63	0.31
Staphylococcus aureus	–	–	–	–	–	–	–	–	–	–	–	–	–	–
Escherichia coli	–	–	–	–	–	–	–	–	–	–	–	–	–	–
Candida albicans	–	–	–	–	–	–	–	4 ± 0.2	1.5 ± 0.5	–	–	–	–	–

be explained by the presence of two tetrazole moieties which, due to its structure, allows the tetrazole derivatives to readily bind to various enzymes or receptors in living organisms via weak interactions such as coordination bonds, hydrogen bonds, hydrophobic effect, π–π stacking, van der Waals force, and so on, leading to a broad spectrum of biological activities [22, 23]. Since *C. albicans* represents a major health issue driven by developments in medical care [24], the discovery and identification of new drugs and treatment approaches represents a major challenge. Within this context, taking into account the proven activity of compound **5**, various strategies could be developed, including combined loading of compound **5** with an antifungal drug (e.g., propiconazole), to improve its capacity to destroy yeast cells [25].

Conclusions

Two new functionalized bimesitylene derivatives containing nitrile and tetrazolyl moieties were synthesized and characterized, and their structural particularities are described and discussed. The crystal packing of compound **4** shows the presence of one-dimensional supramolecular chains running along *b* axis, sustained by weak H-bonding between CH_3 as donors and nitrile groups as acceptors of protons, while in compound **5**, the components of the structure interact via a O–H···N and N–H···O hydrogen-bonding system, forming a three-dimensional supramolecular network.

The computational chemistry approach was applied to compound **5** using DFT with the B3LYP and LSDA methods and 6-31+G** basis set. The optimized molecular geometries were in good agreement with the observed crystal structure, with RMSD goodness-of-fit estimator ≤0.354 Å. The patterns of the frontier molecular orbitals (HOMO, LUMO) indicated obvious delocalization, suggesting a strong π–π conjugated system. Likewise, population analysis, electrostatic potential, dipole moment, bandgap energy (HOMO–LUMO), and global reactivity descriptors were evaluated and are discussed.

The newly synthesized compounds were additionally tested for their antimicrobial activity, revealing that bimesitylene derivative **5** displayed antifungal properties when compared with compound **4**. Even though it can be speculated that the tetrazolyl moieties are responsible for this, further studies are required to elucidate the mechanism of action involved.

Experimental

Materials and instrumentation

All commercially available reagents were used without further purification. All chemicals were purchased in their highest purity grade. Proton and carbon nuclear magnetic resonance (δ_H, δ_C) spectra were recorded on a Bruker Avance DRX 400 MHz spectrometer, equipped with a 5-mm four-nuclei ($^1H/^{13}C/^{19}F/^{29}Si$) direct detection, *z*-gradient probe. Chemical shifts are referenced to the residual solvent signal of dimethylsulfoxide (DMSO)-d6 (^1H: 2.51 ppm; ^{13}C: 39.47 ppm). IR spectra

were recorded on a FTIR Shimadzu or Jasco 660 *plus* FTIR spectrophotometer. Mass spectrometry data were obtained using an Agilent 6520 series Accurate-Mass Quadrupole Time-of-Flight (Q-TOF) LC/MS (positive ion mode). CHN elemental analysis was performed on a Vario-EL-III elemental analyzer. X-ray diffraction measurements were carried out with an Oxford Diffraction XCALIBUR E CCD diffractometer equipped with graphite-monochromated Mo K_α radiation.

Synthesis of bimesitylene 2

Magnesium turnings (0.5 g, 20.6 mmols) were placed in an oven-dried flask, under nitrogen atmosphere. THF (25 mL) was then added, and the mixture was heated to reflux. Mesityl bromide (3 mL, 20 mmols) was then added in small volumes to the reaction flask. The resulting solution was refluxed for 2 h, during which the magnesium reacted completely. After this, a solution of iron chloride (0.3 g, 1.85 mmols) and dibromoethane (1.3 mL, 15 mmols) in diethylether (5 mL) was added dropwise to the reaction flask, and the resulting solution was refluxed for another 3 h. The mixture thus obtained was allowed to cool down to room temperature, and aqueous hydrochloric acid (5%, 5 mL) was then added to it. The solution was then extracted with dichloromethane (3 × 20 mL), the extracts were combined and dried over magnesium sulfate, and the solvent was evaporated. The residue thus obtained was purified over silica gel, using hexane as eluent, yielding bimesitylene as colorless solid (1.4 g, 60%). ^{1}H NMR (400 MHz, $CDCl_3$): δ 2.40 (s, 6H, $2CH_3$), 1.93 (s, 12H, $4CH_3$) ppm. ^{13}C NMR (100 MHz, $CDCl_3$): δ 137.0, 136.0, 135.5, 128.2, 21.2, 19.9 ppm.

Synthesis of 3,3′,5,5′-tetraiodobimesitylene 3

To a solution of bimesitylene (0.5 g, 2 mmols) in chloroform (1 mL), iodine (1.18 g, 4.6 mmols) was added, followed by acetic acid (3 mL) and nitric acid (2 mL). To this mixture, sulfuric acid (2 mL) was then added dropwise, over 15–30 min. The solution thus obtained was stirred vigorously at room temperature for 4 h, after which it was poured over ice–water (100 mL). The precipitate thus obtained was then filtered, air-dried, and recrystallized from chloroform, yielding 3,3′,5,5′-tetraiodobimesitylene as colorless crystals (1.26 g, 85%). ^{1}H NMR (400 MHz, $CDCl_3$): δ 2.40 (s, 6H, $2CH_3$), 1.93 (s, 12H, $4CH_3$) ppm. ^{13}C NMR (100 MHz, $CDCl_3$): δ 137.0, 136.0, 135.5, 128.2, 21.2, 19.9 ppm.

Synthesis of 3,3′,5,5′-tetracyanobimesitylene 4

To a solution of tetraiodobimesitylene (3.71 g, 5 mmols) in DMF (30 mL), copper(I) cyanide (2.5 g, 28 mmols) was added, and the resulting mixture was heated to 140 °C for 24 h. The resulting solution was then cooled down to room temperature and poured over aqueous ammonia (25%, 100 mL). The mixture thus obtained was extracted with dichloromethane (3 × 50 mL), and the extracts were combined and dried over magnesium sulfate. The solvent was then evaporated under reduced

pressure, and the residue was separated over silica gel, using dichloromethane as eluent, yielding the desired compound as colorless solid (1.25 g, 70%). ^{1}H NMR (400 MHz, $CDCl_3$): δ 2.85 (s, 6H, $2CH_3$), 2.17 (s, 12H, $4CH_3$) ppm. ^{13}C NMR (100 MHz, $CDCl_3$): δ 146.5, 144.3, 136.4, 115.4, 114.5, 20.4, 19.4 ppm. IR (ATR, cm^{-1}): 3288 (w), 2926 (m), 2856 (w), 2224 (s), 1767 (w), 1566 (s), 1443 (s), 1381 (s), 1267 (w), 1024 (m), 953 (m), 744 (w), 662 (m). MS (ESI) *m/z* Calcd. for $C_{22}H_{19}N_4$ $[M+H]^+$: 339.1, found: 339.2. Elem. anal. calc. for $C_{22}H_{18}N_4$ (338.1): C 78.08, H 5.36, N 16.56; found: C 78.31, H 5.42, N 16.21.

Synthesis of bistetrazolybimesitylene 5

A suspension of tetracyanobimesitylene (0.68 g, 2 mmols), sodium azide (1.3 g, 20 mmols), and zinc chloride (0.82 g, 6 mmols) in DMF (50 mL) was heated to 150 °C for 72 h. The mixture was then cooled down to room temperature and poured over water (20 mL). The pH of the resulting solution was adjusted to 1–2 using 5% aqueous hydrochloric acid, and the resulting precipitate was filtered and washed thoroughly with water. The washed precipitate was then redissolved in a solution of aqueous ammonia (25%, 1 mL) in water (20 mL), and the pH was once again adjusted to 1–2 using 5% aqueous hydrochloric acid. The newly formed precipitate was then filtered, washed thoroughly with water, and air-dried, yielding the desired product as light-brown powder (0.25 g, 30%). ^{1}H NMR (400 MHz, DMSO-*d6*): δ 16.85 (bs, 2H, 2NH), 2.22 (s, 6H, $2CH_3$), 2.15 (s, 6H, $2CH_3$), 1.61 (s, 6H, $2CH_3$) ppm. ^{13}C NMR (100 MHz, DMSO-*d6*): δ 153.3, 142.5, 141.8, 141.5, 137.1, 125.6, 117.2, 113.3, 19.4, 19.3, 18.3 ppm. IR (ATR, cm^{-1}): 3497 (bs), 2924 (m), 2854 (w), 2750 (w), 2232 (s), 1661 (m), 1580 (s), 1447 (s), 1383 (s), 1244 (s), 1188 (w), 1090 (s), 1051 (s), 964 (s), 741 (w), 631 (w). MS (ESI) *m/z* Calcd. for $C_{22}H_{21}N_{10}$ $[M+H]^+$: 425.1, found: 425.2. Elem. anal. calc. for $C_{22}H_{20}N_{10}$ (424.1): C 62.25, H 4.75, N 33.00; found: C 62.43, H 4.87, N 32.65.

X-ray crystallography

Crystallographic measurements for **4** and **5** were carried out with an Oxford Diffraction XCALIBUR E CCD diffractometer equipped with graphite-monochromated Mo K_α radiation. Single crystals were positioned at 40 mm from the detector, and 240 and 245 frames were measured for 6 and 8 s over 1° scan width for **4** and **5**, respectively. Unit cell determination and data integration were carried out using the CrysAlis package of Oxford Diffraction [26]. The structure was solved by direct methods using Olex2 [27] software with the SHELXS [3] structure solution program and refined by full-matrix least-squares based on and refined by full-matrix least-squares on F^2 with SHELXL-97 [28] using an anisotropic model for nonhydrogen atoms. All H atoms attached to carbon were introduced in idealized positions (d_{CH} = 0.96 Å) using the riding model. Positional parameters of H attached to O and N atoms were obtained from difference Fourier syntheses and verified by the geometric parameters of the corresponding hydrogen bonds. Drawings of molecules were obtained using Olex2 program.

X-ray data for compound 4 $C_{22}H_{18}N_4$, M_r = 338.40 g mol^{-1}, size 0.35×0.30×0.30 mm^3, monoclinic, space group $P2_1/n$, a = 9.8130(9) Å, b = 13.1409(11) Å, c = 14.7753(12) Å, β = 92.706(8)°, V = 1903.2(3) Å^3, Z = 4, ρ_{calcd} = 1.181 g cm^{-3}, μ(Mo K$_\alpha$) = 0.072 mm^{-1}, $F(000)$ = 712, 3372 reflections in h (−11/11), k (−15/9), l (−17/14), measured in the range 4.16° ≤ 2Θ ≤ 50.04°, completeness Θ_{max} = 99.6%, 3372 independent reflections, R_{int} = 0.0460, 241 parameters, 0 restraints, R_{1obs} = 0.0691, wR_{2obs} = 0.1591, R_{1all} = 0.1104, $wR2_{all}$ = 0.1857, GoF = 1.035, largest difference peak and hole: 0.22/−0.22 e A^{-3}. CCDC 1834380.

X-ray data for compound 5 $C_{22}H_{25.1}N_{10}O_{2.55}$, M_r = 470.42 g mol^{-1}, size 0.45×0.30×0.25 mm^3, monoclinic, space group $C2/c$, a = 15.4450(19) Å, b = 15.6184(11) Å, c = 12.9152(10) Å, β = 122.919(7)°, V = 2615.3(4) Å^3, Z = 4, ρ_{calcd} = 1.195 g cm^{-3}, μ(Mo K$_\alpha$) = 0.084 mm^{-1}, $F(000)$ = 990, 5290 reflections in h (−15/18), k (−18/17), l (−15/11), measured in the range 4.08° ≤ 2Θ ≤ 50.06°, completeness Θ_{max} = 99.8%, 2301 independent reflections, R_{int} = 0.0243, 160 parameters, 0 restraints, R_{1obs} = 0.0632, wR_{2obs} = 0.1779, R_{1all} = 0.0771, $wR2_{all}$ = 0.1910, GoF = 1.045, largest difference peak and hole: 0.46/−0.21 e A^{-3}. CCDC 1834382.

Computational protocol

Computer simulations were performed on an HPC cluster using the Gaussian09 package [29] for electronic structure calculations. Computational outputs were analyzed in GaussView5 graphical interface software [30] on a Dell Precision workstation T7910. Density functional theory (DFT) was applied to optimize molecular geometries using the B3LYP and LSDA methods and double-zeta split-valence basis set (6-31+G**). The crystal structure (CIF file) was adopted as input conformation for geometry optimization of the isolated molecule (in gas phase). The optimized geometries exhibited no imaginary frequencies, confirming that they represent minimum-energy structures. For conformational goodness-of-fit analysis, YASARA-Structure software[1] [31] was employed. In addition, the MOPAC program was used for computation of some descriptors at the level of PM7 semiempirical theory [32].

Antimicrobial activity

Antimicrobial activity was determined by disk diffusion bioassays [33] against three different reference strains, viz. *Escherichia coli* ATCC25922, *Staphylococcus aureus* ATCC25923, and *Candida albicans* ATCC10231. All microorganisms were stored at −80 °C in 20% glycerol. The bacterial strains were refreshed in Müller–Hinton broth at 36 °C, and the yeast strain was refreshed on Sabouraud dextrose agar at 36 °C. Microbial suspensions were prepared with these cultures in sterile solution to obtain turbidity optically comparable to that of 0.5 McFarland standards, yielding a suspension containing 1×10^8 colony-forming units (CFU) mL^{-1} for all

[1] http://www.yasara.org—YASARA official site (Yet Another Scientific Artificial Reality Application).

microorganisms. Volumes of 0.5 mL from each inoculum were spread onto Müller–Hinton agar, and the compound was added after drying of the medium surface. A sterilized paper disc (6 mm) was placed on the middle of the plate. An aliquot (50 μL) of **4** and **5** (concentration 20 mg/mL in DMSO) was added on the paper disc. To evaluate the antimicrobial properties, growth inhibition was measured after 24 h of incubation at 36 ± 1 °C. All tests were carried out in triplicate to verify the results. After incubation, the diameters of the inhibition zones were measured.

Acknowledgements Financial support from the European Social Fund for Regional Development, Competitiveness Operational Programme Axis 1—Project "Novel Porous Coordination Polymers with Organic Ligands of Variable Length for Gas Storage," POCPOLIG (ID P_37_707, Contract 67/08.09.2016, cod MySMIS: 104810) is gratefully acknowledged. The research related to computational chemistry is part of a project that has received funding from the European Union's Horizon 2020 research and innovation program under grant agreement no. 667387 WIDESPREAD 2-2014 SupraChem Lab.

References

1. J. Hassan, M. Sevignon, C. Gozzi, E. Schulz, M. Lemaire, Chem. Rev. **102**, 1359 (2002)
2. C. Janiak, J.K. Vieth, New J. Chem. **34**, 2366 (2010)
3. J.N. Moorthy, R. Natarajan, P. Venugopalan, J. Org. Chem. **70**, 8568 (2005)
4. W. Lu, Z. Wei, D. Yuan, J. Tian, S. Fordham, H.C. Zhou, Chem. Mater. **26**, 4589 (2014)
5. J.N. Moorthy, R. Natarajan, G. Savitha, P. Venugopalan, Cryst. Growth Des. **6**(4), 919 (2006)
6. C.X. Wei, M. Bian, G.H. Gong, Molecules **20**, 5528 (2015)
7. K. Adil, Y. Belmabkhout, R.S. Pillai, A. Cadiau, P.M. Bhatt, A.H. Assen, G. Maurin, M. Eddaoudi, Chem. Soc. Rev. **46**, 3402 (2017)
8. L.J. Chen, H.B. Yang, M. Shionoya, Chem. Soc. Rev. **46**, 2555 (2017)
9. L.R. Mingabudinova, V.V. Vinogradov, V.A. Milichko, E. Hey-Hawkins, A.V. Vinogradov, Chem. Soc. Rev. **45**, 5408 (2016)
10. M. Eddaoudi, D.F. Sava, J.F. Eubank, K. Adila, V. Guillerm, Chem. Soc. Rev. **44**, 228 (2015)
11. Y.X. Tan, F. Wang, J. Zhang, Chem. Soc. Rev. **47**, 2130 (2018)
12. V. Karunakaran, V. Balachandran, Spectrochim. Acta A **98**, 229 (2012)
13. A. Suvitha, S. Periandy, S. Boomadevi, M. Govindarajan, Spectrochim. Acta A **117**, 216 (2014)
14. M. Karabacak, E. Sahin, M. Cinar, I. Erol, M. Kurt, J. Mol. Struct. **886**, 148 (2008)
15. I. Sidir, Y.G. Sidir, M. Kumalar, E. Tasal, J. Mol. Struct. **964**, 134 (2010)
16. G. Cahiez, C. Chaboche, F. Mahuteau-Betzer, M. Ahr, Org. Lett. **7**(10), 1943 (2005)
17. M.F. Zaltariov, C. Cojocaru, S. Shova, I. Sacarescu, M. Cazacu, J. Mol. Struct. **1120**, 302 (2016)
18. O.M. Becker, A.D. MacKerell, B. Roux, M. Watanabe, *Conformational Analysis, in Computational Biochemistry and Biophysics* (Marcel Dekker, New York, 2001), pp. 69–90
19. J. Frau, D. Glossman-Mitnik, Molecules **23**(3), 559 (2018)
20. R. Vijayaraj, V. Subramanian, P.K. Chattaraj, J. Chem. Theory Comput. **5**(10), 2744 (2009)
21. C.M. Chang, Y.H. Ou, T.C. Liu, S.Y. Lu, M.K. Wang, SAR QSAR Environ. Res. **27**(6), 441 (2016)
22. L.L. Dai, S.F. Cui, G.L.V. Damu, C.H. Zhou, Chin. J. Org. Chem. **33**, 224 (2013)
23. J. Roh, K. Vavrova, A. Hrabalek, Eur. J. Org. Chem. **31**, 6101 (2012)
24. C.G. Pierce, J.L. Lopez-Ribot, Expert Opin. Drug Discov. **8**(9), 1177 (2013)
25. B. Minea, N. Marangoci, D. Peptanariu, I. Rosca, V. Năstasă, A. Corciova, C.D. Varganici, A. Nicolescu, A. Fifere, A. Neamțu, M. Mareş, M. Bărboiu, M. Pinteală, New J. Chem. **40**, 1765 (2016)
26. CrysAlis RED, Oxford Diffraction Ltd., Version 1.171.36.32, 2003
27. O.V. Dolomanov, L.J. Bourhis, R.J.J. Gildea, A.K. Howard, H. Puschmann, J. Appl. Cryst. **42**, 339 (2009)
28. G.M. Sheldrick, Acta Crystallogr. A **A64**, 112 (2008)
29. M.J. Frisch, G.W. Trucks, H.B. Schlegel, G.E. Scuseria, M.A. Robb, J.R. Cheeseman, G. Scalmani, V. Barone, B. Mennucci, G.A. Petersson, H. Nakatsuji, M. Caricato, X. Li, H.P. Hratchian,

A.F. Izmaylov, J. Bloino, G. Zheng, J.L. Sonnenberg, M. Hada, M. Ehara, K. Toyota, R. Fukuda, J. Hasegawa, M. Ishida, T. Nakajima, Y. Honda, O. Kitao, H. Nakai, T. Vreven, J.A. Montgomery, J.E. Peralta, F. Ogliaro, M. Bearpark, J.J. Heyd, E. Brothers, K.N. Kudin, V.N. Staroverov, R. Kobayashi, J. Normand, K. Raghavachari, A. Rendell, J.C. Burant, S.S. Iyengar, J. Tomasi, M. Cossi, N. Rega, J.M. Millam, M. Klene, J.E. Knox, J.B. Cross, V. Bakken, C. Adamo, J. Jaramillo, R. Gomperts, R.E. Stratmann, O. Yazyev, A.J. Austin, R. Cammi, C. Pomelli, J.W. Ochterski, R.L. Martin, K. Morokuma, V.G. Zakrzewski, G.A. Voth, P. Salvador, J.J. Dannenberg, S. Dapprich, A.D. Daniels, Ö. Farkas, J.B. Foresman, J.V. Ortiz, J. Cioslowski, D.J. Fox, *Gaussian 09* (Gaussian Inc., Wallingford, CT, 2009)

30. R. Dennington, T. Keith, J. Millam, *GaussView, Version 5* (Semichem Inc., Shawnee Mission, KS, 2009)
31. E. Krieger, G. Vriend, Bioinformatics **30**, 2981 (2014)
32. J.J.P. Stewart, J. Mol. Model. **19**, 1 (2013)
33. D.F. Brown, D. Kothari, J. Clin. Pathol. **28**, 779 (1975)